Low-Temperature Water-Assisted Oxidation of Sponge-Like Zn Nanostructures for Environmental and Energy Harvesting Applications

Original
Low-Temperature Water-Assisted Oxidation of Sponge-Like Zn Nanostructures for Environmental and Energy Harvesting Applications / Laurenti, M; Fontana, M; Stassi, S; Sacco, A; Scalia, A; Bianco, S; Pirri, Cf; Lamberti, A. - In: ADVANCED MATERIALS INTERFACES. - ISSN 2196-7350. - 10:36(2023). [10.1002/admi.202300485]

Publisher:
WILEY

Published
DOI:10.1002/admi.202300485

Low-Temperature Water-Assisted Oxidation of Sponge-Like Zn Nanostructures for Environmental and Energy Harvesting Applications

Marco Laurenti, Marco Fontana, Stefano Stassi, Adriano Sacco, Alberto Scalia, Stefano Bianco, Candido F. Pirri, and Andrea Lamberti*

In this work, the oxidation of sponge-like nanostructured Zn films exploiting their interaction with water in liquid and vapor phases is investigated. By simply exposing the sputtered porous metal layers to a water vapor atmosphere or incubating them in water at different temperatures, the full conversion to ZnO is obtained. Depending on the kind of treatment, the oxidized ZnO layers exhibit different morphologies and physico-chemical properties. When in combination with low heating of the surface, a better crystallinity and the growth of hexagonal nanocrystals (nanoprisms and nanoflowers) from the nanobranched Zn structure is observed, preserving the sponge-like morphology of the starting material. Good photocatalytic activities for the degradation of an organic dye are measured under simulated sunlight irradiation. The piezoelectric and semiconducting response of the oxidized ZnO layers is also examined, revealing appealing performance in both cases and envisaging their use as nanogenerators and photoanode material in dye-sensitized solar cells. The multifunctional properties of the oxidized ZnO film are discussed in terms of the selected water oxidation approach that tune the corresponding morphology and crystallinity. The low-temperature oxidation approaches here proposed allow the fabrication of flexible semiconductive ZnO films highly desirable in different fields of nanoelectronics.

1. Introduction

Among the main issues faced by the World in the XXI century, energy savings and production from renewable sources, and the alarming problem of environmental pollution, are surely the most compelling ones. For these reasons, there is an urgent need to develop new technological solutions, both from the materials science and engineering standpoints, able to produce and harvest energy from renewable resources, but also to degrade pollutants often present in a wide plethora of hazardous wastes such as air, wastewater, and seawater.

With the advent of nanomaterials, strong efforts have been devoted to the study of innovative multifunctional materials featuring the above-mentioned properties. In this scenario, zinc oxide (ZnO) has captured considerable attention thanks to its intriguing physical properties and the easiness of material synthesis.

ZnO is a wide band-gap semiconducting material showing UV light absorption, piezoelectric, and photocatalytic properties.[1,2] ZnO can be simply prepared by following various synthesis approaches, that range from wet-chemistry methods like the sol-gel and hydrothermal ones,[3] to physical and chemical vapor deposition strategies such as sputtering[4] and atomic layer deposition[5] to name a few.

In the specific contest of thin-film morphology, valuable examples have shown that ZnO nanostructuration can be simply achieved and tuned by acting on the deposition route and parameters: arrays of nanowires,[6,7] nanorods,[8,9] nanofibers,[10] nanotubes,[11] and several more complex structures[12] can be produced, and the respective physical and chemical properties change accordingly to the shape of the selected ZnO nanostructure. For example, it is easy to obtain enormous electron transport properties and improved piezoelectric charge generation using ZnO nanowire arrays,[13,14] while superior gas sensing skills can be observed testing ZnO films with a flower-like morphology.[15,16] However, some of the most interesting ZnO properties, like the optical and electrical ones, can be

---

M. Laurenti, M. Fontana, S. Stassi, A. Scalia, S. Bianco, C. F. Pirri, A. Lamberti
Department of Applied Science and Technology
Politecnico di Torino
C.so Duca degli Abruzzi 24, Torino 10129, Italy
E-mail: Stefano.stassi@polito.it

A. Sacco, C. F. Pirri, A. Lamberti
Center for Sustainable Future Technologies @Polito
Istituto Italiano di Tecnologia
Via Livorno, 60, Torino 10144, Italy

The ORCID identification number(s) for the author(s) of this article can be found under https://doi.org/10.1002/admi.202300485

DOI: 10.1002/admi.202300485

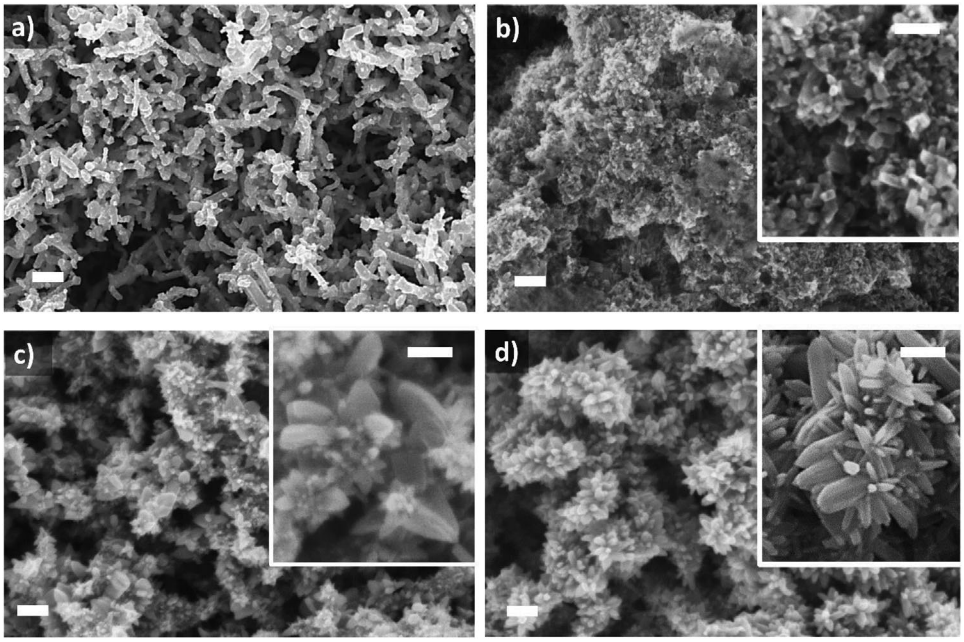

Figure 1. a) Top-view FESEM images of sputtered Zn layer; b) ZnO-Water sample, prepared after incubation in water at room temperature for 48 h; c) ZnO-Boiled sample, obtained after incubation at 90 °C for 4 h; d) ZnO-Vapor sample, obtained after the exposition to water vapor for 2 h. The scale bars correspond to 200 nm for low-magnification images and 100 nm for high-magnification images in the insets.

negatively influenced by the presence of intrinsic defects like zinc interstitials and oxygen vacancies.[17] Hence, even when a low-temperature synthesis method was chosen, a thermal treatment was required to reduce ZnO defectiveness and obtain the desired properties. We have recently proposed a simple and scalable method to fabricate sponge-like ZnO films on several substrates by combining sputtering and thermal oxidation.[18,19] In this case, a relatively low temperature (i.e., 380°C) is exploited to convert the metal Zn nanostructure into the oxide counterpart.[20,21] In this optics, the introduction of low-temperature, water-assisted treatments could reduce the oxidative temperature down to ambient one. This approach has attracted huge interest in the scientific community, in particular, related to the crystallization of amorphous TiO_2 nanotube into anatase phase[22–24] or as a method to synthesize metal oxide nanostructures applicable to a wide range of elemental metals, including Zn.[25] However, in the latter case, the shape and uniformity of the resulting ZnO nanostructures are dictated by the crystal structure and surface roughness of the Zn metal foil used as the starting raw material.

Here, we demonstrate for the first time the water-assisted oxidation of sputtered Zn sponge-like nanostructures by room temperature incubation in water and by other water-assisted treatments, and their use in various applications related to energy storage and environmental application. The ZnO samples were characterized in order to understand the oxidative mechanism and the multifunctional properties of these nanostructures. The results show promising photovoltaic conversion of water-treated ZnO electrodes. The semiconducting nature of the water-oxidized ZnO layers, combined with the particular morphology and surface chemistry also envisage their application as photocatalytic material for dye degradation. Finally, the charge generation properties of the ZnO nanostructured layers have been evaluated under mechanical deformation. All the results are discussed in terms of the specific morphology and crystal structure characterizing the considered ZnO nanostructure and their correlation with the particular wet oxidation approach.

2. Results and Discussion

2.1. Morphological, Structural, and Surface Chemistry Analysis of Nanostructured ZnO Layers

The morphology of sputtered Zn layers and the low-temperature, water-assisted oxidized ZnO ones has been assessed by means of Field Emission Scanning Electron Microscopy (FESEM) analyses. **Figure 1**a shows the peculiar sponge-like morphology of the starting metallic Zn layer, featuring elongated, nanometer-sized grains interconnecting each other and forming a branched and porous network. On the other side, Figure 1b–d shows the morphology of the ZnO samples after the water-assisted oxidation process. It is found that the ZnO-Water sample (Figure 1b) is formed mainly by the coalescence of fine nanocrystals whose shape highly resembles the one observed for the grains of the starting Zn layer. In the case of ZnO-Boiled and ZnO-Vapor samples a different morphology is observed, with the growth of ordered crystalline nanostructures like nanoprisms (Figure 1c) and nanoflowers (Figure 1d).

The different morphology of the oxidized samples with respect to the non-oxidized ones is due to the water-assisted oxidation treatment, which can be described as a corrosion mechanism. The interaction of a metal surface exposed to water vapor is a highly complex process, involving three different phases, i.e., the gas, liquid, and solid ones, and their corresponding interfaces (solid/liquid, liquid/gas, and solid/gas). Moreover, the

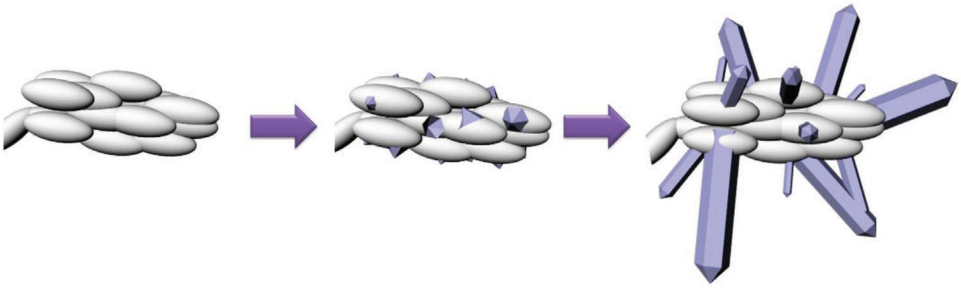

Figure 2. Sketch of the growing mechanism leading to the formation of the particular morphology observed for ZnO-Vapor and ZnO-Boiled samples, during the corresponding low-temperature, water-vapor oxidation treatments.

nanostructuration of the metal increases the complexity of the reaction, thereby influencing the oxidation rate. Leygraf and coworkers[26,27] have extensively investigated the corrosion mechanism of zinc exposed to water vapor at room temperature. Even though their studies are devoted to understanding atmospheric corrosion, the same approach can be useful to describe the low-temperature oxidation herein proposed. The exposure of the metal oxide surface to the water vapor leads to the formation of a thin water film with a thickness on the order of some nanometers that corresponds to the reversible adsorption and desorption of water from the zinc surface.[27] This aqueous adlayer is the medium in which the corrosion reaction occurs. Afterward, electrochemistry drives the atmospheric corrosion process through the Zn/Zn^{2+} and O_2/H_2O redox couples. There are anodic regions, where the zinc ions are released, and cathodic sites, where the electrons are consumed by forming hydroxide ions.[26] The oxidation process can be described by the subsequent chemical and electrochemical reactions:

$$\mathrm{Zn} \rightarrow \mathrm{Zn}^{2+} + 2\mathrm{e}^{-} \quad (1)$$

$$1/2\mathrm{O}_2 + \mathrm{H}_2\mathrm{O} + 2\mathrm{e}^{-} \rightarrow 2\mathrm{OH}^{-} \quad (2)$$

$$\mathrm{Zn}^{2+} + 2(\mathrm{OH})^{-} \rightarrow \mathrm{Zn(OH)}_2 \rightarrow \mathrm{ZnO} + \mathrm{H}_2\mathrm{O} \quad (3)$$

In their studies, Leygraf and coworkers[27] found out that the formed ZnO is quite uniform, with grains being 10–100 nm in size and forming a layer with a final average thickness of ≈50 nm after 72 h. Instead in our case, the full conversion to ZnO is obtained after only 2 h of exposure to water vapor. This increase in the oxidation rate can be ascribed to the huge, exposed surface area of the sponge-like Zn nanostructure coupled with the light heating of the substrate (≈50°C) provided during the water oxidation treatment. In particular, the effect of temperature on the final morphology of water-oxidized ZnO is more evident for ZnO-Vapor and ZnO-Boiled samples, in which the heating of the starting Zn layer is expected to play a major role than for ZnO-Water sample, due to the different experimental conditions. A 3D sketch of the growing mechanism leading to the formation of such a more-ordered ZnO morphology featuring well-defined nanoprims and nanoflowers is provided in **Figure 2**.

Figure 3a shows the XRD patterns of the sputtered Zn layer and the ZnO samples prepared by exploiting the low-temperature oxidation treatments described previously. Independently of the oxidation method, the XRD patterns clearly highlight the conversion of the starting Zn layer into the oxide counterpart. Actually, the starting Zn layer shows multiple diffraction peaks belonging to (002), (100), and (101) crystal planes of the metallic Zn phase (Joint Committee on Powder Diffraction Standard (JCPDS) database, card no. 87–0713). On the other hand, all the ZnO samples crystallized in the hexagonal wurtzite structure and showed intense diffraction peaks positioned at ≈31.8°, 34.4°, and 36.2° belonging to (100), (002), and (101) crystal planes, respectively (JCPDS card no. 89–1397). Minor diffraction peaks due to reflections coming from other ZnO crystal planes are also detected at higher 2θ angles. No residual crystallographic phases of the starting Zn layer are detected; thus, a complete oxidation of the metallic layer is obtained after each of the low-temperature oxidation treatments exploited in this work. There are also some minor contributions from the FTO substrate, which are identified in accordance with the JCPDS card no. 88–0287. Calculated reference spectra for the FTO, Zn, and ZnO phases are provided in (Figure S1, Supporting Information).

Further information on the microstructure of the ZnO films is obtained by Rietveld refinement of the XRD patterns (see Supporting Information for the details). The refined cell parameters are provided in **Table 1**, alongside the estimated crystallite size and micro-strain.

Concerning the lattice parameters, the ZnO-Water film shows slightly smaller lattice parameters with respect to the ZnO-Boiled and ZnO-Vapor samples, which in turn have comparable values within the estimated uncertainties. The same trend is also displayed by the crystallite size, which is significantly higher (≈29 and ≈33 nm) for the samples oxidized at higher temperature (ZnO-Boiled and ZnO-Vapor) in comparison with the ZnO-Water film (≈20 nm). The estimation of the crystallite size is important for its possible correlation with the functional properties: for example, it has been shown that larger crystallite size may result in enhanced piezoelectric response.[12] Although micro-strain is

Table 1. Rietveld refined values for the lattice parameters of the ZnO unit cell (a, c), crystallite size, and micro-strain. The uncertainties on the refined parameters are written in parenthesis and they refer to the last digit.

SAMPLE	a [Å]	c [Å]	size [nm]	micro-strain
ZnO-Water	3.248 (1)	5.207 (1)	20 (1)	/
ZnO-Boiled	3.254 (1)	5.212 (1)	29 (1)	/
ZnO-Vapor	3.253 (1)	5.211 (1)	33 (1)	0.0011 (1)

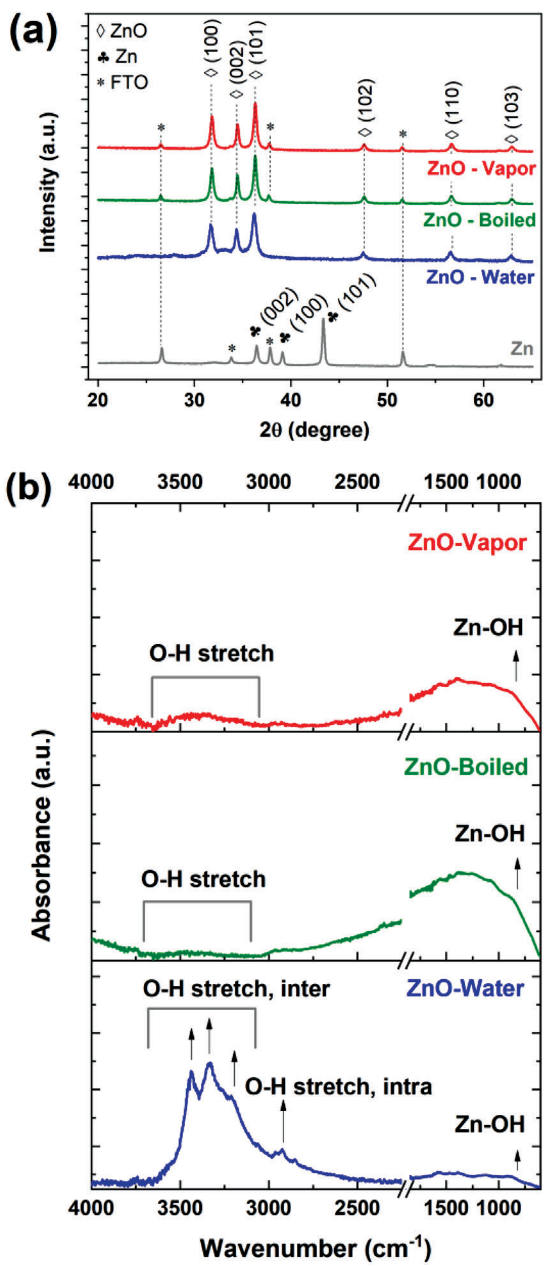

Figure 3. a) XRD pattern of sputtered Zn layer and of ZnO films oxidized exploiting the above-discussed treatments: water vapor, incubation in water at room temperature and at 90 °C. b) ATR-IR spectra collected on the ZnO-Vapor, ZnO-Boiled, and ZnO-Water samples.

usually common in nanocrystalline materials,[28] the only sample where this effect is significant (i.e., not comparable with 0 within the estimated uncertainty) is ZnO-Vapor: this could be a consequence of the complex oxidation mechanism involving three different phases, as previously discussed. Based on the refinement of the relative intensities of the diffraction peaks, it is also possible to investigate preferred orientation in the ZnO films with an exponential harmonic model.[29] Figure S2 (Supporting Information) provides the refinement results, alongside the simulation of rotationally-symmetric pole figures based on the exponential harmonic expansion. The calculated pole figures provide visualization in stereographic projection of the presence of preferred orientation along the direction perpendicular to the surface of the sample for the (100) and (002) crystallographic family of planes for all the ZnO samples. The preferred orientation of the (002) planes is particularly interesting for charge generation applications, since for ZnO the piezoelectric response is enhanced along the direction perpendicular to the (002) family of planes.

ATR-IR spectra of the nanostructured ZnO layers are shown in Figure 3b. In the case of ZnO-Boiled and ZnO-Vapor samples, the presence of a broad IR band due to O—H stretching mode is noticed in the range 3500–3000 cm^{-1}. This band is fairly visible for ZnO-Boiled sample while it appears more pronounced for ZnO-Vapor sample. On the other hand, a stronger IR band in the same wavenumber region is found for ZnO-Water sample, with the appearance of well-defined and distinct IR peaks positioned at ≈3436, 3330, and 3219 cm^{-1}, assigned to asymmetric/symmetric stretching vibrations of intermolecular O—H bonds in water molecule. Additional IR contributions belonging to O—H stretching vibration and due to intramolecular bonds are also detected in the range 2950–2850 cm^{-1}. An IR peak positioned at ≈3750 cm^{-1} and due to water of crystallization is also visible for all the samples. The presence of the ZnO layer is confirmed by a broad band in the range 950–850 cm^{-1} and due to Zn—OH mode. The increase in O—H vibration band intensity observed only for ZnO-Water sample is ascribed to the increased adsorbed water due to the particular oxidation approach, that involved the direct contact of the metallic Zn layer with water at room temperature for 48 h.

2.2. Photocatalytic Properties

The photocatalytic behavior of the different ZnO samples has been studied by evaluating the degradation of Rhodamine-β dye under simulated sunlight irradiation conditions. The degradation efficiency of the dye over time is shown in **Figure 4**a, while Figure S3 (Supporting Information) summarizes the time evolution of UV absorption spectra for Rh-β dye solution collected at different points of time. Without the presence of the ZnO catalyst, the dye degradation is almost negligible during time. For ZnO-Vapor and ZnO-Boiled samples, ≈50% dye degradation is found after 4 h of irradiation. ZnO-Water sample shows a slightly better degradation efficiency, approaching 60%. Independently of the considered sample, the degradation profile follows a pseudo-first-order kinetic law (Figure 4b), with a kinetic constant k (h^{-1}) of 0.083, 0.125, and 0.183 for ZnO-Vapor, ZnO-Boiled, and ZnO-Water samples, respectively.

The observed degradation of Rh-β in presence of the catalyst can be explained by considering the semiconducting nature of ZnO under UV illumination conditions. This behavior results from the ability of valence band electrons to overcome the energy band-gap when excited by photon absorption and fill conduction band states (free conduction electrons). This transition occurs during the photocatalytic experiments: the interaction between the photogenerated free conduction electrons and the hydroxyl groups present in the water-based solution generates •OH radical species able to react with Rh-β molecule and determine its degradation. The mechanism of Rh-β degradation is ascribed to

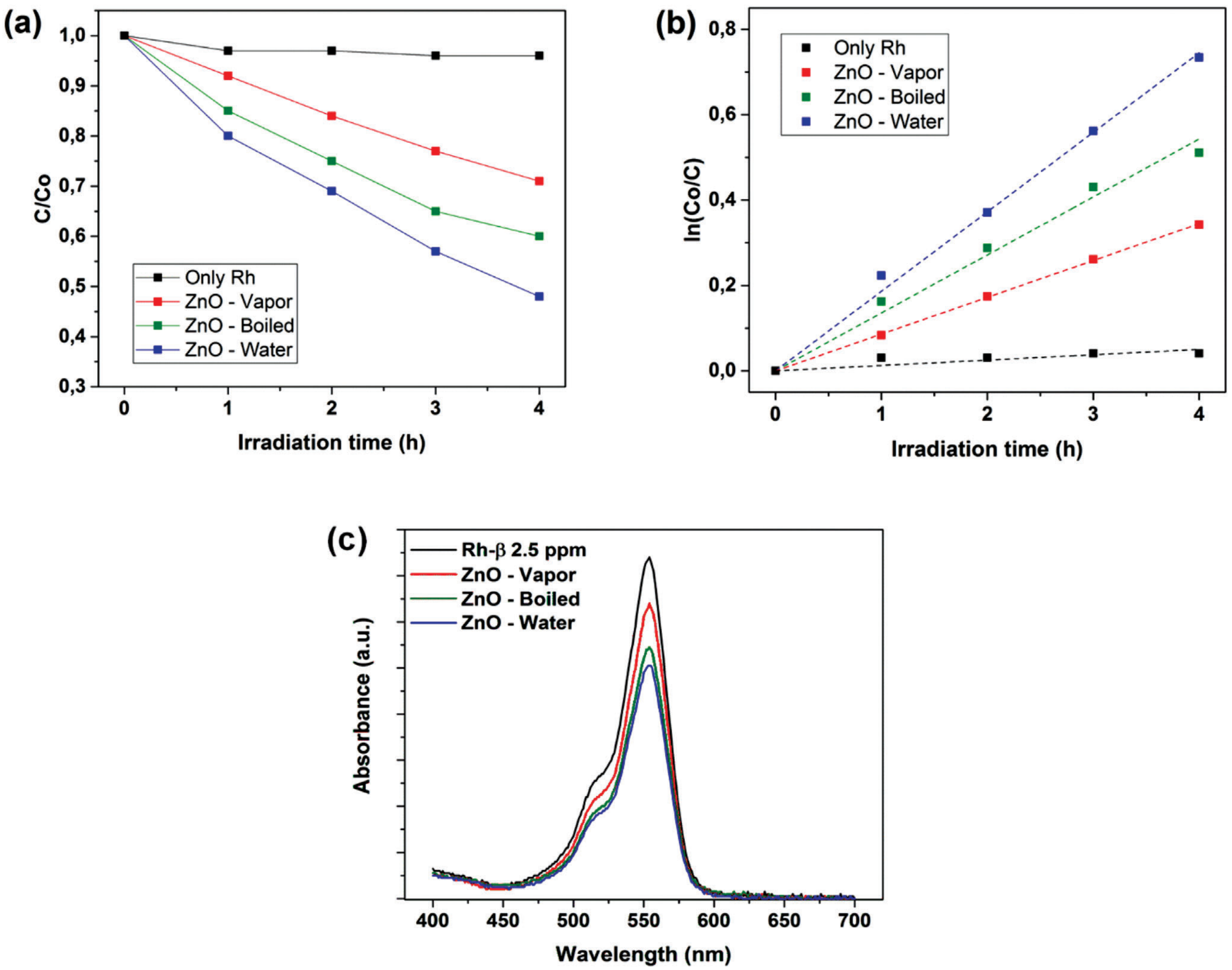

Figure 4. a,b) Photodegradation profiles of Rhodamine-β dye versus irradiation time, for the different water-oxidized ZnO layers. Fitting curves are presented as dashed lines. Control experiments ("Only Rh") were performed without the presence of the ZnO catalyst by using FTO covered glasses. c) UV absorption spectra for Rhodamine-β dye solution representing the different dye adsorption properties of ZnO-Vapor, ZnO-Boiled, and ZnO-Water samples at the end of the dark phase (20 min).

de-ethylation process and the cleavage of chromophore xanthene group.[30] For de-ethylation process, a shift of the characteristic UV absorption peak of Rh-β is observed, while the cleavage of the chromophore xanthene group is represented by a strong reduction of the UV peak intensity. Since no shift of the UV peak position has been observed, while the reduction of the absorption peak intensity has been detected in all the cases (see Figure S2, Supporting Information), the dominant mechanism in all our degradation experiments is the cleavage of the chromophore xanthene group.

To further understand the difference in the photocatalytic behavior among the different samples, the amount of dye adsorbed on the various photocatalytic substrates has been qualitatively assessed by considering the UV spectra of Rh-β solution collected at the end of the dark phase (Figure 4c). The maximum reduction in the UV peak intensity is obtained for ZnO-Water sample. The IR results shown in Figure 3b highlight a greater presence of hydroxyl groups for ZnO-Water sample compared to ZnO-Vapor and ZnO-Boiled samples. Hydroxyls are negatively-charged surface groups that act as reaction sites for dye absorption. Therefore, the slightly better degradation efficiency of ZnO-Water sample is related to its hydroxyl-rich surface chemistry, that highly promotes the adsorption of the dye on the outermost catalyst surface and its following degradation during illumination.

Even though the complete degradation of the dye has never been achieved in our experiments, the photodegradation efficiency of the organic dye measured in this work (≈60% of degradation after 4 h) is comparable or even better than those reported in other works for pure ZnO-based photocatalysts.[31] For example, a good photodegradation efficiency of Rh-β under simulated sunlight has been demonstrated for commercial ZnO powders after 30 min of irradiation.[32] Despite the kinetic of degradation being faster than in our case, the best results in terms of photodegradation efficiency did not exceed 40%. Lower efficiencies have been reported for the degradation of methylene blue (13.9% after 210 min irradiation time) and methyl orange (20%

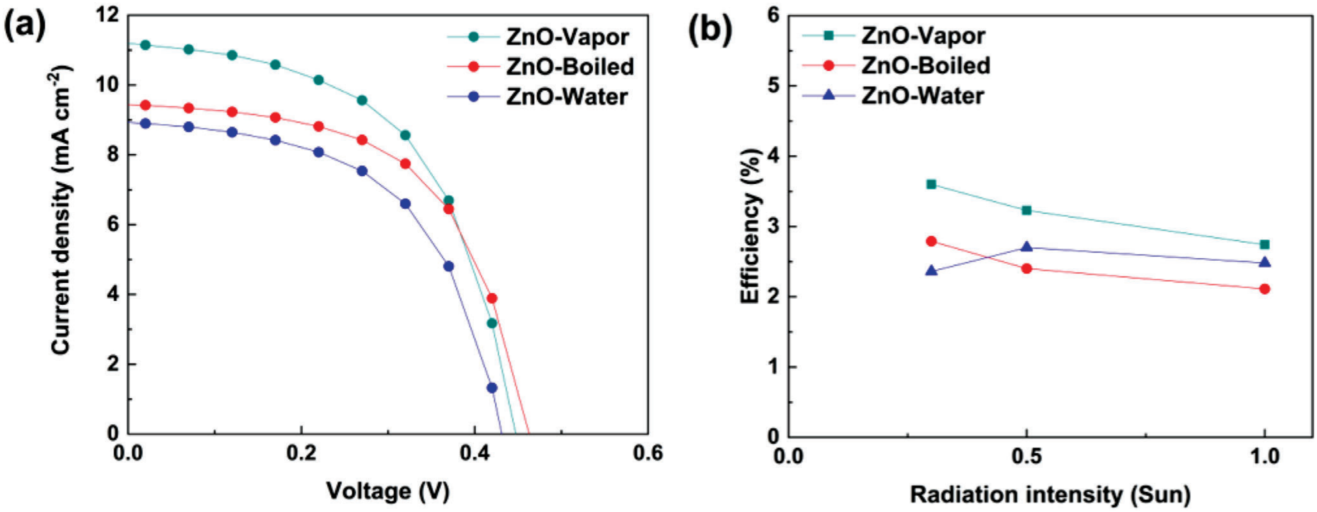

Figure 5. a) Current density-voltage curves under 1 sun AM1.5 irradiation obtained for DSSCs based on low temperature water assisted oxidized ZnO photoanodes. b) Corresponding photoconversion efficiencies obtained at different radiation intensities.

after 100 min irradiation time) by using ZnO nanofibers[33] and nanoparticles,[34] respectively.

Generally, the limited photodegradation efficiency of pure ZnO is inferred to the corresponding electro-optical properties. It is well-known that ZnO-based materials show excellent light absorption in the UV region,[35] that represents only 5% of sunlight spectrum, i.e., the light source used in our photocatalytic experiments. On the contrary, light absorption of ZnO in the visible-near infrared range is quite limited. Another drawback of ZnO is its intrinsic n-type conducting behavior. Once free carriers (electrons and holes) are photogenerated, their recombination can rapidly occur and lowers the photodegradation efficiency of the catalyst. Both the limitations, i.e., the wide energy bandgap and fast recombination of the photogenerated carriers, can be successfully mitigated by doping ZnO with selected elements.[36] The photocatalytic study discussed in this work deals with the use of pristine ZnO-based catalysts under simulated sunlight illumination. Therefore, the limited degradation efficiency is expectable as only the UV portion of light could be effectively absorbed from the ZnO catalysts and converted into catalytically-active photogenerated electrons, whose effectiveness can be reduced by charge recombination phenomena.

2.3. Sponge-Like ZnO Nanostructured Layers as Photoanode Material for Dye Sensitized Solar Cells

The *I–V* curves of the different ZnO-based Dye Sensitized Solar Cells (DSSCs) under 1 sun illumination conditions are reported in **Figure 5**a, while the calculated photovoltaic parameters are resumed in Table S1 (Supporting Information). All the samples, whose thickness is ≈8 μm, exhibit short circuit current densities (J_{sc}) in the range 9–11 mA cm^{-2} and open circuit voltages of ≈0.45 V, leading to photoconversion efficiencies (PCEs) in the range 2–3%. These values are typical of ZnO-based DSSCs,[37–40] which are characterized by lower performance with respect to state-of-the-art TiO$_2$-based devices.[40] With respect to our previous work,[41] the increase of the exposure time to water vapor up to 2 h resulted to be beneficial to the PV performance of the ZnO-Vapor cell, as witnessed by the larger J_{sc} and PCE values. Moreover, by illuminating this device with lower intensity (Figure 5b), it can be possible to increase the PCE up to 3.7%, making this cell promising for indoor PV application.[42] This enhancement is due to the decrease in charge recombination, given the minor presence of photogenerated electrons in the conduction band.[43] The same holds for ZnO-Boiled DSSC. On the contrary, ZnO-Water device does not exhibit any increase of efficiency under low-illumination conditions. This outcome may be explained considering the smaller size of nanoparticles in this sample compared to the others (see Table 1): this leads to a higher density of surface defects (grain boundaries, etc.) that act as recombination centers, thus making the electronic transport more difficult and thus limiting the efficiency of this device under low-illumination conditions. It is important to highlight that the ZnO-Vapor DSSC exhibits the largest currents among all the devices. This behavior can be associated to the higher crystallinity of this sample, which can guarantee higher charge transport properties.[21] This result was confirmed by measuring the conductivity of the samples, which was found to be equal to 3.75, 0.88, and 0.25 mS cm^{-1} for vapor, boiled, and water samples, respectively.

2.4. Charge Generation from Sponge-Like ZnO Nanostructured Layers

Piezoeletric properties of the different ZnO nanostructured layers were evaluated by a direct mode, thus by measuring the generated charges induced by a mechanical deformation. In order to exploit the ZnO samples to harvest energy also from very small strain, a set-up based on an automatic syringe pump to induce very small deformation by the fall of water droplets was used (**Figure 6**a), as already described elsewhere.[44,45] The impact on the surface of piezoelectric ZnO structures produces a

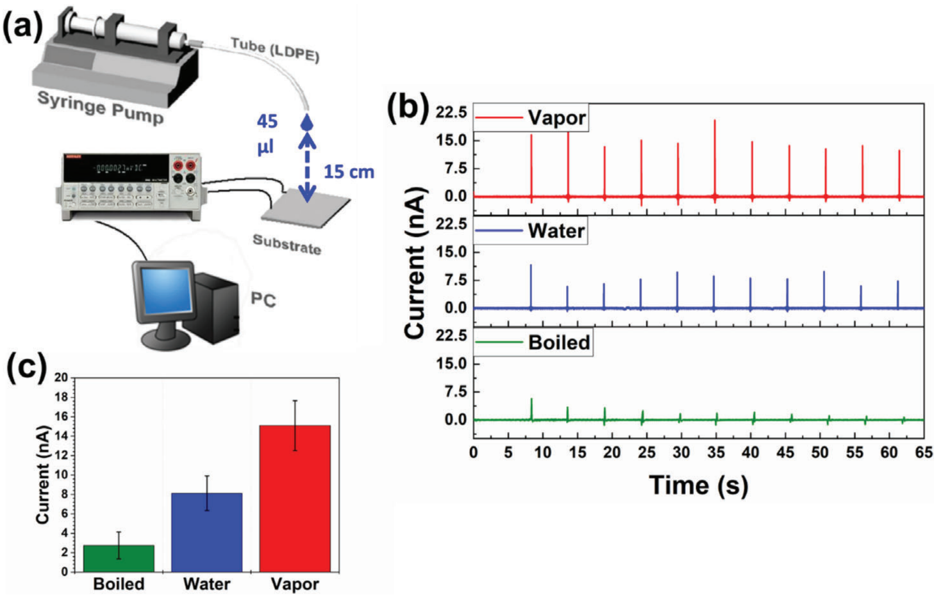

Figure 6. a) Scheme of the set-up used for piezoelectric current generation under the deformation induced by water droplets. b) Current peaks generated by the three different ZnO samples in time and c) average values of the generated current peaks.

compressive deformation and thus the generation of an impulse of charges, measured as a fast current peak. The positive part of the peak is related to the compression induced by the splash of the water, while the small negative part to the release of the elastic mechanical deformation. The very small deformation induced by the splash of the drop on the piezoelectric material was however able to produce an appreciable current generation of the order of tens on nanoampere (Figure 6b). The highest values of current generation were reached by ZnO-Vapor sample with an average of 15 ± 3 nA (Figure 6c). The better performances of the vapor-oxidized sample were expected, since it reports the higher level of crystallinity and bigger grain size, as observed previously from XRD data discussion. Indeed, piezoelectricity is a phenomenon highly dependent on the crystalline phase of a material; a bigger crystals size enhances the piezoelectric phenomenon, while the presence of several grain boundaries damps the piezoelectric response.[12] These results, together with the photovoltaic measurements, confirm that water-vapor oxidized ZnO is the best candidate for energy harvesting applications.

3. Conclusion

Nanostructured ZnO films have been prepared by a low-temperature, water-assisted oxidation of metallic, sponge-like Zn layers deposited by sputtering. The morphology, the crystallinity and the surface chemistry of the resulting ZnO surface could be tuned by following three different oxidation approaches, namely the exposure to water vapor and its incubation in water at room temperature and 90 °C. Elongated, highly interconnected nanocrystalline grains resembling the starting Zn morphology are found after water incubation at room temperature. On the other hand, oxidation into mild-temperature conditions (incubation into hot water and exposition to water vapors) promotes the growth of a more crystalline structure composed by nanoprisms and nanoflowers. XRD and IR results show that all the fabricated ZnO samples crystallize in the hexagonal wurtzite phase and present a hydroxyl-rich surface chemistry. Some differences can be observed among the samples: oxidation at mild temperature conditions favor a better crystallinity, while the direct incubation of the samples in water results into a hydroxyl-richer surface, thanks to the direct contact of the metallic Zn with water rather than the exposition to vapors. The multifunctional properties of the developed ZnO film were assessed in terms of photocatalytic degradation of an organic dye, piezoelectric charge generation and photoelectron conversion efficiency when used as photoanode material in DSSCs. Among all the ZnO film, superior crystallinity-driven properties in terms of piezoelectric charge generation and photoelectron conversion efficiencies were achieved when the exposition to water vapors of the metallic Zn surface was exploited. On the other side, after direct incubation in water at room temperature, the oxidized ZnO film shows the best trade-off between surface chemistry properties and crystallographic quality, which finally improves the photocatalytic response. Overall, our findings demonstrate how the low-temperature water oxidation approaches herein proposed are simple, green, scalable and low-cost methods to develop highly-nanostructured ZnO surfaces that can be integrated as multifunctional active materials in light-weight semiconducting devices for environmental, energy savings and recovery applications.

4. Experimental Section

Preparation of Sponge-Like ZnO Layers: Sponge-like ZnO nanostructures were obtained by a simple two-step method. Zinc (Zn) films were first deposited by radio frequency (RF) magnetron sputtering technique. Then, the conversion of the metallic Zn layer into ZnO was obtained by a low temperature water-oxidation method performed into different conditions as described in the following. Fluorine-doped Tin Oxide (FTO) covered glasses (7 Ω sq^{-1}, Solaronix) were used as transparent conductive substrates. Before the deposition, all the substrates were washed with acetone and ethanol in an ultrasonic bath and then with a Piranha solution (sulfuric acid and hydrogen peroxide in 3:1 volume ratio). The substrates were properly covered with a hard mask to define the desired geometry for the final photoanode fabrication (0.78 cm^2). The sputtering deposition process was discussed in detail previously.[19,46] Briefly, metallic Zn films were obtained starting from a 4 inch diameter Zn target, facing downward the FTO substrates. The target-to-substrate distance was maintained fixed at ≈8 cm and no intentional heating was provided to the substrates during the overall sputtering deposition process. Before starting the deposition, suitable high-vacuum conditions (2×10^{-7} Torr) were obtained by a two-stage pumping system. A RF signal (working frequency 13.56 MHz, power density 0.66 W cm^{-2}) was applied to the cathode and used to create plasma conditions. The deposition process was performed in inert Ar atmosphere, with a fixed gas pressure of 5×10^{-3} Torr. The deposition time was set to 2 h. In order to prevent the incorporation of contaminants, the Zn target was pre-cleaned with a sputtering process performed for 15 min.

After the deposition, the Zn-coated FTO substrates were converted into ZnO by following three different low-temperature oxidation approaches. In the first case ("ZnO-Water"), the Zn samples were incubated into De-Ionized (DI)-water (18 Mω cm^{-1}) at 25 °C for 48 h. In the second case ("ZnO-Vapor"), the Zn samples were fixed into a clamping system and exposed for 2 h to the water vapor deriving from DI-water heated at 90 °C. In the third case ("ZnO-Boiled"), the Zn-coated FTO samples were treated into hot water for 4 h heated on a hot plate. The temperature of the substrates was monitored by a Pt100 controller.

Fabrication of DSSCs Based on Nanostructured ZnO Photoanodes: For photoanode preparation, all the ZnO sample typologies were heated at 70 °C and soaked into a 0.175 mM N719 dye solution (Ruthenizer535bis-TBA, Solaronix) in ethanol for 2 h at room temperature and then rinsed in ethanol to remove the un-adsorbed dye molecules.[20,40] The counter electrodes were made by FTO-covered glasses coated with a 5 nm Pt layer deposited by thermal evaporation.[20,40] Dye-sensitized Solar Cells (DSSCs) were assembled using a microfluidic architecture[47] using a liquid I^-/I^{3-} redox couple electrolyte (Iodolyte AN50, Solaronix).

Characterization Techniques: Field-Emission Scanning Electron Microscopy (FESEM) analysis was performed with a ZEISS AURIGA dual beam FIB–FESEM microscope. The crystalline structure of the samples was investigated by means of X-ray diffraction (XRD) with a Panalytical X'Pert PRO diffractometer working in $\theta - 2\theta$ configuration and equipped with a Cu Kα ($\lambda = 1.54059$ Å) X-ray radiation source. MAUD software[48] was used for full XRD pattern fitting based on the Rietveld method. Attenuated Total Reflectance Infrared (ATR-IR) spectroscopy was carried out with a Nicolet 5700 FTIR spectrometer from ThermoFisher. All of the spectra were background subtracted and acquired with 2 cm^{-1} resolution and 64 scan accumulation. The assignment of IR modes was done according to Ref. [49].

The PV characteristics of the ZnO-based DSSCs were obtained with a Keithley 2440 SMU, employing a Newport 91195A class A solar simulator (AM1.5G illumination, 1000 W m^{-2}). Different radiation intensities were provided to the cells in order to evaluate their photoconversion efficiencies under diverse illumination conditions (namely 0.3, 0.5, and 1 suns), employing Neutral Density filters (Newport).

The photocatalytic properties of the ZnO layers were investigated by studying the degradation of an organic dye (Rhodamine-β, Rh-β) under simulated sunlight irradiation conditions. Rh-β powder (1 mg) was dissolved in bidistilled water (final volume 400 mL), under continuous stirring at room temperature and in dark conditions. A calibration curve for Rh-β UV absorbance intensity versus concentration was determined by considering the characteristic UV absorbance of Rh-β at $\lambda = 554$ nm obtained from various solutions prepared at prefixed dye concentrations. The photodegradation experiments were performed using a sun simulator lamp system working at 1 sun (Class A, Newport, 500 W). Before starting each degradation experiment, the lamp was calibrated by using a commercial Si photovoltaic cell as reference. The ZnO-coated FTO glass samples were placed atop of a Teflon support within a cylindrical Pyrex reactor and soaked in the Rh-β solution (volume 10 mL, concentration 2.5 ppm), under continuous magnetic stirring (350 rpm).[50] The temperature of the system (dye solution + photocatalyst) was kept constant at 25 °C during the overall experiment by placing the reactor inside a water-bath cooling system. Before irradiating, the ZnO samples were left in contact with Rh-β solution in dark conditions under continuous stirring for 20 min, in order to achieve adsorption–desorption equilibrium conditions between dye and the photocatalyst. The photocatalytic efficiency and kinetic of degradation of the photocatalyst were determined according to Ref. [50].

Piezoelectric measurements of the ZnO nanostructured layers were performed by a direct mode, thus by measuring the generated charges induced by a mechanical deformation. A home-made set-up based on an automatic moto-syringe for the generation of water droplets and a Low Current Electrometers for current generation evaluation (Keithley 6517b) was used. The ZnO samples were packaged with a flexible top electrode composed of a copper metalized polymide foil, then water and electrically insulated by means of a polyimide adhesive tape. The samples were then connected to the low current electrometer to evaluate the current upon the repetitive fall of water drops, hitting the material surface. The samples were mounted with an angle of 30° with respect of the perpendicular to the water drops trajectory to avoid water accumulation on the surface. Indeed, water droplets of ≈45 µL (i.e., 45 µg) were dispensed by the automatic syringe pump at a height of 15 mm from the sample surface.

Supporting Information

Supporting Information is available from the Wiley Online Library or from the author.

Conflict of Interest

The authors declare no conflict of interest.

Author Contributions

M.L. and M.F. contributed equally to this work.

Data Availability Statement

The data that support the findings of this study are available from the corresponding author upon reasonable request.

Keywords

dye-sensitized solar cells, low temperature syntheses, photocatalytic properties, piezoelectric charge generation, sponge-like nanostructures, water-assisted oxidations, zinc oxide

Received: June 12, 2023
Revised: August 29, 2023

---

[1] L.-Z. Kou, W.-L. Guo, C. Li, *2008 Symposium on Piezoelectricity, Acoustic Waves, and Device Applications* **2008**, *354*.
[2] S. Sakthivel, B. Neppolian, M. V. Shankar, B. Arabindoo, M. Palanichamy, V. Murugesan, *Sol. Energy Mater. Sol. Cells* **2003**, *77*, 65.
[3] A. Kolodziejczak-Radzimska, T. Jesionowski, *Materials* **2014**, *7*, 2833.

[4] Y. Wang, C. Wang, Z. Peng, Q. Wang, X. Fu, *Surf. Rev. Lett.* **2017**, *24*, 1850006.
[5] D. Kim, H. Kang, J. M. Kim, H. Kim, *Appl. Surf. Sci.* **2011**, *257*, 3776.
[6] M. Laurenti, A. Verna, M. Fontana, M. Quaglio, S. Porro, *Appl. Phys. A: Mater. Sci. Proc.* **2014**, *117*, 901.
[7] M. Laurenti, A. Verna, M. Fontana, S. Stassi, G. Canavese, S. L. Marasso, V. Cauda, *Adv. Mater. Interfaces* **2016**, *3*, 1600110.
[8] Q. Ahsanulhaq, J.-H. Kim, Y.-B. Hahn, *Nanotechnology* **2007**, *18*, 485307.
[9] L. V. Podrezova, V. Cauda, S. Stassi, G. Cicero, K. A. Abdullin, B. E. Alpysbaeva, *Cryst. Res. Technol.* **2014**, *49*, 599.
[10] J. Y. Park, S. S. Kim, *J. Am. Ceram. Soc.* **2009**, *92*, 1691.
[11] A. B. F. Martinson, J. W. Elam, J. T. Hupp, M. J. Pellin, *Nano Lett.* **2007**, *7*, 2183.
[12] V. Cauda, S. Stassi, A. Lamberti, M. Morello, C. Fabrizio Pirri, G. Canavese, *Nano Energy* **2015**, *18*, 212.
[13] M. Law, L. E. Greene, J. C. Johnson, R. Saykally, P. Yang, *Nat. Mater.* **2005**, *4*, 455.
[14] Z. L. Wang, J. S. Song, *Science* **2006**, *312*, 242.
[15] S. G. Ansari, R. Wahab, Z. A. Ansari, Y.-S. Kim, G. Khang, A. Al-Hajry, H.-S. Shin, *Sens. Actuators, B* **2009**, *137*, 566.
[16] T. Krishnakumar, R. Jayaprakash, N. Pinna, N. Donato, A. Bonavita, G. Micali, G. Neri, *Sens. Actuators, B* **2009**, *143*, 198.
[17] L. Schmidt-Mende, J. L. MacManus-Driscoll, *Materstoday* **2007**, *10*, 40.
[18] R. Gazia, G. Canavese, A. Chiodoni, A. Lamberti, S. Stassi, A. Sacco, S. Bianco, A. Virga, E. Tresso, C. F. Pirri, *J. Alloys Compd.* **2014**, *586*, S331.
[19] R. Gazia, A. Chiodoni, S. Bianco, A. Lamberti, M. Quaglio, A. Sacco, E. Tresso, P. Mandracci, C. F. Pirri, *Thin Solid Films* **2012**, *524*, 107.
[20] A. Lamberti, R. Gazia, A. Sacco, S. Bianco, M. Quaglio, A. Chiodoni, E. Tresso, C. F. Pirri, *Prog. Photovoltaics* **2014**, *22*, 189.
[21] A. Sacco, A. Lamberti, R. Gazia, S. Bianco, D. Manfredi, N. Shahzad, F. Cappelluti, S. Ma, E. Tresso, *Phys. Chem. Chem. Phys.* **2012**, *14*, 16203.
[22] T. Miyasaka, *J. Phys. Chem. Lett.* **2011**, *2*, 262.
[23] S. Senthilarasu, T. A. N. Peiris, J. García-Cañadas, K. G. U. Wijayantha, *J. Phys. Chem. C* **2012**, *116*, 19053.
[24] V. Zardetto, F. Di Giacomo, D. Garcia-Alonso, W. Keuning, M. Creatore, C. Mazzuca, A. Reale, A. Di Carlo, T. M. Brown, *Adv. Energy Mater.* **2013**, *3*, 1292.
[25] N. S. Saadi, L. B. Hassan, T. Karabacak, *Sci. Rep.* **2017**, *7*, 7158.
[26] J. Hedberg, J. Henriquez, S. Baldelli, C. M. Johnson, C. Leygraf, *J. Phys. Chem. C* **2009**, *113*, 2088.
[27] P. Qiu, D. Persson, C. Leygraf, *J. Electrochem. Soc.* **2009**, *156*, C81.
[28] A. Stukowski, J. Markmann, J. Weissmüller, K. Albe, *Acta Mater.* **2009**, *57*, 1648.
[29] P. Van Houtte, *Textures Microstruct.* **1991**, *13*, 199.
[30] T. Rasheed, M. Bilal, H. M. N. Iqbal, H. Hu, X. Zhang, *Water, Air Soil Pollution* **2017**, *228*, 291.
[31] K. M. Lee, C. W. Lai, K. S. Ngai, J. C. Juan, *Water Res.* **2016**, *88*, 428.
[32] O. Haibo, H. J. Feng, L. Cuiyan, C. Liyun, F. Jie, *Mater. Lett.* **2013**, *111*, 217.
[33] M. Samadi, H. A. Shivaee, A. Pourjavadi, A. Z. Moshfegh, *Appl. Catal., A* **2013**, *466*, 153.
[34] S. Sun, X. Chang, X. Li, Z. Li, *Ceram. Int.* **2013**, *39*, 5197.
[35] M. Yin, Y. Gu, I. L. Kuskovsky, T. Andelman, Y. Zhu, G. F. Neumark, S. O'Brien, *JACS* **2004**, *126*, 6206.
[36] B. Ghanbari Shohany, A. Khorsand Zak, *Ceram. Int.* **2020**, *46*, 5507.
[37] J. A. Anta, E. Guillén, R. Tena-Zaera, *J. Phys. Chem. C* **2012**, *116*, 11413.
[38] D. Pugliese, F. Bella, V. Cauda, A. Lamberti, A. Sacco, E. Tresso, S. Bianco, *ACS Appl. Mater. Interfaces* **2013**, *5*, 11288.
[39] E. Puyoo, G. Rey, E. Appert, V. Consonni, D. Bellet, *J. Phys. Chem. C* **2012**, *116*, 18117.
[40] N. Shahzad, F. Risplendi, D. Pugliese, S. Bianco, A. Sacco, A. Lamberti, R. Gazia, E. Tresso, G. Cicero, *J. Phys. Chem. C* **2013**, *117*, 22778.
[41] A. Lamberti, A. Sacco, M. Laurenti, M. Fontana, C. F. Pirri, S. Bianco, *J. Alloys Compd.* **2014**, *615*, S487.
[42] A. Sacco, L. Rolle, L. Scaltrito, E. Tresso, C. F. Pirri, *Appl. Energy* **2013**, *102*, 1295.
[43] J. C. Chou, C. H. Kuo, P. Y. Kuo, C. H. Lai, Y. H. Nien, Y. H. Liao, C. C. Ko, C. M. Yang, C. Y. Wu, *IEEE J. Photovoltaics* **2019**, *9*, 926.
[44] G. Canavese, S. Stassi, V. Cauda, A. Verna, P. Motto, A. Chiodoni, S. L. Marasso, D. Demarchi, *IEEE Sens. J.* **2013**, *13*, 2237.
[45] R. Gazia, P. Motto, S. Stassi, A. Sacco, A. Virga, A. Lamberti, G. Canavese, *Nano Energy* **2013**, *2*, 1294.
[46] M. Laurenti, G. Canavese, S. Stassi, M. Fontana, M. Castellino, C. F. Pirri, V. Cauda, *RSC Adv.* **2016**, *6*, 76996.
[47] A. Lamberti, A. Sacco, S. Bianco, E. Giuri, M. Quaglio, A. Chiodoni, E. Tresso, *Microelectron. Eng.* **2011**, *88*, 2308.
[48] L. Lutterotti, S. Matthies, H.-R. Wenk, A. S. Schultz, J. W. Richardson, *J. Appl. Phys.* **1997**, *81*, 594.
[49] G. Socrates, in *Infrared and Raman Characteristic Group Frequencies: Tables and Charts*, John Wiley & Sons, NJ, USA **2004**.
[50] M. Laurenti, N. Garino, G. Canavese, S. Hernandéz, V. Cauda, *ACS Appl. Mater. Interfaces* **2020**, *12*, 25798.